

## Nonlinear gain dynamics of quantum dot optical amplifiers

This article has been downloaded from IOPscience. Please scroll down to see the full text article.

2011 Semicond. Sci. Technol. 26 014008

(<http://iopscience.iop.org/0268-1242/26/1/014008>)

View [the table of contents for this issue](#), or go to the [journal homepage](#) for more

Download details:

IP Address: 130.149.114.144

The article was downloaded on 24/11/2010 at 15:01

Please note that [terms and conditions apply](#).

# Nonlinear gain dynamics of quantum dot optical amplifiers

Miriam Wegert<sup>1</sup>, Niels Majer<sup>1</sup>, Kathy Lüdge<sup>1</sup>, Sabine Dommers-Völkel<sup>2</sup>, Jordi Gomis-Bresco<sup>2</sup>, Andreas Knorr<sup>1</sup>, Ulrike Woggon<sup>2</sup> and Eckehard Schöll<sup>1</sup>

<sup>1</sup> Institut für Theoretische Physik, Technische Universität Berlin, 10623 Berlin, Germany

<sup>2</sup> Institut für Optik und Atomare Physik, Technische Universität Berlin, 10623 Berlin, Germany

Received 1 June 2010, in final form 12 September 2010

Published 24 November 2010

Online at [stacks.iop.org/SST/26/014008](http://stacks.iop.org/SST/26/014008)

## Abstract

In this work, the ultrafast gain dynamics of a quantum dot (QD)-based semiconductor optical amplifier (SOA) is modeled on the basis of semiconductor Bloch equations that include microscopically calculated nonlinear scattering rates between QD carriers and the surrounding carrier reservoir. This enables us to separately study the dynamics of electrons and holes inside the device as well as the coherent effects related to the fast polarization dynamics. We show that the optical pulse power and the dephasing time of the polarization mainly affect the gain depletion inside the active region, while the electric injection current density and thus the internal carrier dynamics influence the gain recovery. We observe that carrier–carrier scattering is the source of desynchronized behavior of electrons and holes in the recovery dynamics of QD-based SOAs. The amplification of pulse trains in the SOA predicted by our model agrees well with experimental data.

(Some figures in this article are in colour only in the electronic version)

## 1. Introduction

Quantum dot (QD)-based semiconductor optical amplifiers (SOAs) are an important optoelectronic application of self-organized QD structures [1]. They are excellent candidates for high-speed data and telecom applications providing ultrafast gain dynamics and pattern effect-free amplification [2–5].

In this paper, we investigate the ultrafast gain recovery of QD SOAs and its underlying carrier dynamics using a quantum mechanical approach on the basis of the semiconductor Bloch equations [6]. The modeling of pump–probe experiments with optical pulses on femtosecond time scales makes it crucial to include the fast decaying polarization [7] and thus to go beyond standard rate equation models for the SOA [8, 9]. Based on previous works about QD lasers [10–15], we include the strongly nonlinear character of electron–electron scattering processes between the QD ground state and the two-dimensional carrier reservoir which is modeled by a 4 nm thick InGaAs layer. The acronym QW (quantum well) is used for the carrier reservoir (instead of the former acronym WL used in our previous works [13–15]) in order to avoid confusion with the more common notion of a mono-molecular wetting layer. Compared to Gomis-Bresco *et al* [7] who used

constant QW carrier densities within a system-bath approach, we include the full carrier dynamics inside the QW described by separate microscopically based rate equations for electrons and holes [13]. Thus, our model allows us to comprehensively study the carrier dynamics inside the device and understand the nonlinear gain dynamics of the SOA without the need of external fit parameters. Propagation effects of the electric field which would otherwise be considered within a traveling wave equation [16] are not taken into account. In a traveling wave approach, access to the full spatiotemporal dynamics of the system and especially the electric field would allow further analysis regarding, e.g. pulse shaping or phase dynamics. These issues are beyond the scope of this work focussing on a detailed analysis of the local response of the gain medium. We also do not incorporate excited states or inhomogeneous broadening in our simulations.

The paper is organized as follows. After introducing the semiconductor Bloch equations in section 2, we analyze the influence of the pulse area  $\theta$ , the dephasing time  $T_2$  and the injection current density  $j$  on the gain dynamics of the QD SOA and compare with experimental results in section 3. We investigate the effect of pulse trains on the gain medium in section 4, before we conclude in section 5.

## 2. Semiconductor Bloch equations

Modeling the gain dynamics of an electrically driven QD SOA in response to an ultra-short optical pulse (see the schematic sketch in figure 1) requires taking into account all dynamic variables that vary on the respective time scales. Since the experimentally observed ultrafast gain recovery occurs on a fs time scale, we include the microscopic polarization  $p$  with a dephasing time  $T_2 \approx 25$  fs as a dynamic variable. Thus, our model describing the SOA uses a quantum mechanical approach based on the semiconductor Bloch equations [6]. Combined with microscopically based rate equations for the carrier densities inside the carrier reservoir (QW) [13], we arrive at the following set of five coupled dynamical equations for the microscopic polarization  $p$ , the occupation probabilities of electrons  $f_e$  and holes  $f_h$  in the QD and the electron and hole densities in the QW  $w_e$  and  $w_h$ , respectively:

$$\dot{p} = -i\frac{\Omega}{2}[f_e + f_h - 1] - \frac{1}{T_2}p, \quad (1)$$

$$\dot{f}_e = -\text{Im}[\Omega(t)p^*] + S_e^{\text{in}}(1 - f_e) - S_e^{\text{out}}f_e - R_{sp}, \quad (2)$$

$$\dot{f}_h = -\text{Im}[\Omega(t)p^*] + S_h^{\text{in}}(1 - f_h) - S_h^{\text{out}}f_h - R_{sp}, \quad (3)$$

$$\dot{w}_e = \eta\frac{j(t)}{e_0} - N^{\text{sum}}[S_e^{\text{in}}(1 - f_e) - S_e^{\text{out}}f_e] - R_{\text{loss}}, \quad (4)$$

$$\dot{w}_h = \eta\frac{j(t)}{e_0} - N^{\text{sum}}[S_h^{\text{in}}(1 - f_h) - S_h^{\text{out}}f_h] - R_{\text{loss}}. \quad (5)$$

Equations (1)–(3) form the semiconductor Bloch equations in rotating wave approximation (RWA) for resonant excitation, while equations (4) and (5) describe the carrier dynamics inside the 2D carrier reservoir. The microscopic polarization  $p$  corresponds to the probability amplitude for an optical transition and is thus a dimensionless quantity.  $\Omega(t) = \mu E(t)/\hbar$  is the Rabi frequency with dipole moment  $\mu$  and slowly varying envelope of the electric field  $E(t)$ . The full complex electric field is given by  $\mathcal{E}(t) = \frac{1}{2}E(t)(e^{i\omega_L t} + e^{-i\omega_L t})$ , where  $\omega_L$  is the carrier wave frequency which we assume to be in resonance with the optical transition energy  $h\nu$  inside the QDs (see the energy diagram in figure 1). The Rabi frequency  $\Omega$  is a measure for the strength of the coupling between light and microscopic polarization (light–matter interaction). In this framework, the induced processes of absorption and emission are modeled by the term  $i\frac{\Omega}{2}[f_e + f_h - 1]$  (see equation (1)). Note that the dynamic equations (1)–(5) do not contain the spatiotemporal evolution of the electric field inside the device because propagation effects are not considered. Instead we describe the local response of the gain medium to an optical input pulse with an envelope function  $E(t) = E_0\frac{1}{\sigma\sqrt{2\pi}}\exp(-\frac{t^2}{2\sigma^2})$  modeled by a Gaussian with variance  $\sigma^2$ . We assume  $E(t)$  to be real and polarized perpendicularly to the propagation direction. Throughout this work, we use Gaussian input pulses for the electric field amplitude  $E(t)$  with a full width at half maximum (FWHM) of 300 fs corresponding to  $\sigma = 127.4$  fs. Note that for fixed FWHM the pulse area  $\theta = \int \Omega(t) dt$  directly scales with the amplitude  $E_0$  of the Gaussian pulse. The spontaneous emission in the QDs is given by  $R_{sp} = Wf_e f_h$ ,

where  $W = \frac{\mu^2\sqrt{\epsilon_{bg}}}{3\pi\epsilon_0\hbar}\left(\frac{\omega}{c}\right)^3$  is the Einstein coefficient with static relative permittivity of the background medium  $\epsilon_{bg}$ , vacuum permittivity  $\epsilon_0$  and vacuum speed of light  $c$ . Further,  $j$  is the current density that is electrically injected into the QW,  $e_0$  is the elementary charge and  $\eta = 1 - w_e/N^{\text{QW}}$  is a current injection efficiency factor reducing the pump efficiency if carriers are already inside the carrier reservoir (maximum density inside the QW:  $w_e = N^{\text{QW}}$ ). The QD density  $N^{\text{sum}}$  is twice the total QD density as given by experimental surface measurements (the factor 2 accounts for spin degeneracy).

Scattering-induced dephasing of the polarization is given by a decay rate  $1/T_2$  in equation (1). A range of values of  $1/T_2$ , strongly depending on the excitation conditions, have been proposed in the literature. Under high excitation, as considered throughout this work, we assume dephasing processes to be strong and therefore choose a small value for  $T_2 = 25$  fs in accordance with experimental measurements [7]. In addition, we investigate the dependence on  $T_2$  in a range between 10 and 100 fs in section 3.2 in order to gain insight into the parameter dependence of the gain dynamics. The phase-destroying scattering processes, e.g. carrier–carrier and carrier–phonon scattering, are stronger for higher temperature; therefore, the dephasing time decreases with increasing temperature [17].  $S_e^{\text{in}}(S_h^{\text{in}})$  and  $S_e^{\text{out}}(S_h^{\text{out}})$  describe the rates of electron (hole) scattering into and out of the QD levels, respectively. Figure 2(a) shows their nonlinear dependence on the QW carrier densities. Because these rates are important for the gain dynamics, they are discussed in more detail at the end of this section.

Losses inside the QW are given by  $R_{\text{loss}} = Bw_e w_h$ . In previous works on QD lasers [13, 14],  $B$  was implemented as a constant bimolecular recombination coefficient. Here, we have extended this by considering Auger recombination inside the QW [18] where the rate varies with the third order in the QW carrier density, in addition to bimolecular recombination processes [19, 20]. Hence, we use  $B = B^S + B^A w_e$ . As a consequence, the time scale  $\tau_e^{\text{QW}}$  of carrier losses inside the QW ( $R_{\text{loss}} = w_e/\tau_e^{\text{QW}}$ ) depends strongly on the carrier densities inside the QW. Figure 2(b) depicts  $\tau_e^{\text{QW}}$  at steady-state laser operation as a function of the normalized injection current density  $j/j_0$ .  $j_0$  denotes the injection current density at transparency which is determined by zero inversion, i.e.,  $f_e + f_h - 1 = 0$ . It can be seen that a higher injection current leads to a drastic decrease of the electron lifetime  $\tau_e^{\text{QW}}$  because of the increasing carrier density (a dashed line in figure 2(b)).

The non-radiative carrier–carrier scattering rates  $S_e^{\text{in}}(S_h^{\text{in}})$  and  $S_e^{\text{out}}(S_h^{\text{out}})$  describing electron (hole) scattering into and out of the QD-levels, respectively, are microscopically calculated as a sum in  $k$ -space over all possible Auger transitions between QW and QD [13]:

$$S_e^{\text{in}} = \sum_{klmb'} W_{klmb'}^{\text{in}} f_k f_l (1 - f_m) \quad (k \rightarrow QD, l \rightarrow m)$$

$$S_e^{\text{out}} = \sum_{klmb'} W_{klmb'}^{\text{out}} (1 - f_k)(1 - f_l) f_m \quad (QD \rightarrow k, m \rightarrow l),$$

where the transition probabilities  $W_{klmb'}^{\text{in/out}}$  contain the screened Coulomb matrix elements and the energy-conserving  $\delta$ -function [10, 12].  $f_k, f_l$  and  $f_m$  are the occupation probabilities

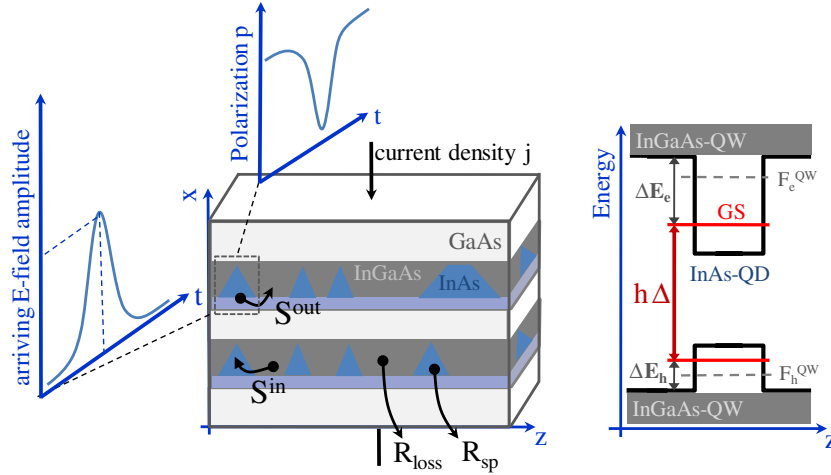


**Figure 1.** Schematic picture of the QD SOA and associated energy diagram (right) of the QD and QW systems.

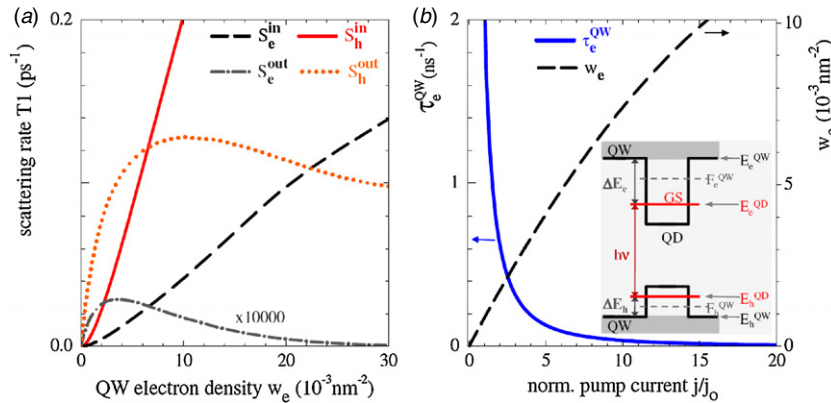


**Figure 2.** (a) Carrier-carrier scattering rates calculated for the QD energy levels shown in the inset of (b) for  $w_h = 1.5w_e$ . Black dashed and gray dash-dotted curves are electron in and out scattering rates, respectively. Red solid and orange dotted curves are hole in and out scattering rates, respectively. (b) Steady-state QW electron density (right axis) and QW electron lifetime  $\tau_e^{\text{QW}} = (Bw_h)^{-1}$  (left axis) as a function of normalized injection current  $j/j_0$ . Inset: associated energy diagram of the QD and QW systems.

of the respective QW states. Assuming quasi-equilibrium within each of the four ensembles of carriers, the in- and out-scattering rates are related via detailed balance [13]:

$$S_e^{\text{in}} = S_e^{\text{out}} \exp \left\{ \frac{F_e^{\text{QW}} - E_e^{\text{QD}}}{kT} \right\}, \quad (6)$$

$$S_h^{\text{in}} = S_h^{\text{out}} \exp \left\{ \frac{E_h^{\text{QD}} - F_h^{\text{QW}}}{kT} \right\}. \quad (7)$$

In the above equations,  $E_e^{\text{QD}}$  and  $E_h^{\text{QD}}$  are the confined QD electron and hole energy levels, respectively, as depicted in the energy diagram of figure 1. The quasi-Fermi levels  $F_b^{\text{QW}}$  for electrons ( $b = e$ ) and holes ( $b = h$ ) in the QW depend on the QW carrier densities  $w_b$ . They are given by

$$F_e^{\text{QW}}(w_e) = E_e^{\text{QW}} + kT \ln \left[ \exp \left( \frac{w_e}{\rho_e kT} \right) - 1 \right], \quad (8)$$

$$F_h^{\text{QW}}(w_h) = E_h^{\text{QW}} - kT \ln \left[ \exp \left( \frac{w_h}{\rho_h kT} \right) - 1 \right], \quad (9)$$

where  $E_e^{\text{QW}}$  and  $E_h^{\text{QW}}$  are the QW band edges of conduction and valence bands as shown in the inset of figure 2(b),  $k$

is the Boltzmann constant and  $T$  is the temperature. The 2D densities of states in the QW given by  $\rho_b = m_b/(\pi\hbar^2)$  depend on the effective masses of electrons and holes  $m_b$ . Introducing the energy differences  $\Delta E_e = E_e^{\text{QW}} - E_e^{\text{QD}}$  and  $\Delta E_h = E_h^{\text{QD}} - E_h^{\text{QW}}$  (see table 1), the relation between in- and out-scattering rates can be expressed as

$$S_b^{\text{in}}(w_e, w_h) = S_b^{\text{out}}(w_e, w_h) e^{\Delta E_b/kT} [e^{w_b/(\rho_b kT)} - 1]. \quad (10)$$

It should be noted that because of the 2D electron gas inside the carrier reservoir the ratio between in and out scattering is not just a constant Boltzmann factor as widely used in the literature, but a term that depends upon the QW carrier density. The resulting nonlinear scattering rates used for the simulations are shown in figure 2(a) exhibiting a pronounced maximum in the out scattering rates (orange dotted and grey dash-dotted line) while the in scattering rates (red solid and black dashed line) increase monotonically.

The values of the parameters used for the simulation are listed in table 1. The parameters are taken from experimental data except for the Einstein coefficient  $W$  and the recombination coefficients  $B^S$  and  $B^A$  which were calculated. The value of the transparency injection current density  $j_0$  is extracted from numerical simulations.

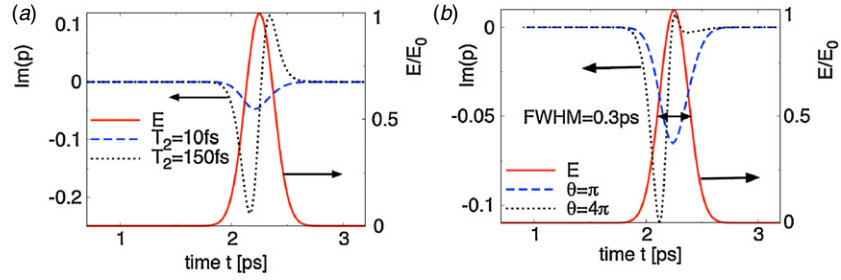


**Figure 3.** Time series of the microscopic polarization  $p(t)$  resulting from (a) an optical input pulse with  $\theta = 2\pi$  simulated for  $T_2 = 10$  fs and  $T_2 = 150$  fs as dashed blue and dotted black lines, respectively ( $j = 20 j_0$ ) and (b) optical input pulses with  $\theta = \pi$  and  $\theta = 4\pi$  shown as dashed blue and dotted black lines ( $T_2 = 25$  fs,  $j = 20 j_0$ ). Solid red curves in (a) and (b): electric field amplitude  $E(t)$  normalized to the maximum  $E_0$ .

**Table 1.** Numerical parameters used in the simulation unless stated otherwise.

Symbol	Value	Symbol	Value
$W$	$0.7 \text{ ns}^{-1}$	$N^{\text{sum}}$	$20 \times 10^{10} \text{ cm}^{-1}$
$T$	$300 \text{ K}$	$N^{\text{QW}}$	$2 \times 10^{13} \text{ cm}^{-1}$
$\mu$	$0.6 e_0 \text{ nm}$	$\Delta E_e(\Delta E_h)$	$210(50) \text{ meV}$
$\varepsilon_{bg}$	$14.2$	$m_e(m_h)$	$0.043(0.45) m_0$
$T_2$	$25 \text{ fs}$	$j_0$	$4220 \text{ mA cm}^{-2}$
$B^S$	$0.03 \text{ nm}^2 \text{ ps}^{-1}$	$B^A$	$305 \text{ nm}^4 \text{ ps}^{-1} \omega_e$

### 3. Full dynamic simulation of single pulses

In the experimental part of the paper, we show differential transmission measurements on a QDs-in-a-well-based SOA to characterize its gain dynamics. The sample studied in this work is a p-i-n structure with a 1 mm long, 2  $\mu\text{m}$  wide waveguide. The active medium consists of 15 layers of MBE-grown QDs-in-a-well with a nominal areal density of  $2 \times 10^{10} \text{ cm}^{-2}/\text{layer}$ . Concretely, we use the heterodyne pump and probe technique, described in detail in [7]. In such a setup, a sufficiently strong pump-pulse (0.1 pJ per pulse, 150 fs full width half maximum) is followed by a delayed weak probe pulse (with an intensity 100 times smaller). Both beams are resonant in energy to the ground state of the quantum dots ( $\lambda = 1.3 \mu\text{m}$ ). The pump pulse induces a gain change of the device, and the probe pulse measures the delayed gain state. By varying the delay time  $\tau$ , the local gain recovery dynamics inside the device can be approximated by the normalized gain defined as

$$g(\omega, \tau) = -\omega \text{Im} \left( \frac{P_{\text{pump+probe}}(\omega, \tau) - P_{\text{pump}}(\omega)}{\mathcal{E}_{\text{probe}}(\omega)} \right). \quad (11)$$

Here,  $P_{\text{pump+probe}}(\omega)$  and  $P_{\text{probe}}(\omega)$  are the Fourier amplitudes of the macroscopic polarizations for the case of both pump and probe and only probe pulse passing through the device, respectively, and  $\mathcal{E}_{\text{probe}}(\omega)$  is the Fourier amplitude of the full complex electric field  $\mathcal{E}(t)$  of the probe pulse. Because the dynamic variable  $p(t)$  determined by equation (1) describes the microscopic polarization inside one QD, the macroscopic polarization  $P(t)$  is obtained by summing the product of microscopic polarization and dipole moment  $\mu$  over all QDs giving  $P(t) = N^{\text{sum}} \mu p(t)$ . Since the slowly varying envelope approximation was applied to

the microscopic polarization  $p(t)$ , the Fourier amplitude of the macroscopic polarization is given by  $P(\omega) = \delta(\omega_0 - \omega) \int P(t) dt$  with  $\omega_0$  being the frequency of the optical transition inside the QDs. As said before we assume to resonantly excite the QD SOA ( $\omega_0 \approx \omega_L$ ). Thus, we can neglect the frequency dependence and use a normalized gain  $g(\tau) \equiv g(\omega_L, \tau)$  to characterize the gain recovery.

To illustrate the basic mechanisms of the gain dynamics, the time evolution of the microscopic polarization  $p(t)$  of the gain medium after being exposed to an optical input pulse with electric field amplitude  $E(t)$  is discussed in the following. Note that equations (1)–(3) have an oscillatory solution with  $p(t) \sim e^{i\Omega t}$  if constant amplitude  $E(t) = E_0$ , zero damping of the polarization, i.e.  $T_2 = \infty$ , and zero scattering and zero spontaneous emission in the carrier equations are assumed. Thus, in this case, polarization and carrier inversion are periodic functions with period  $T = 2\pi/\Omega$  which is called a *Rabi cycle*. For our case of an electric input pulse with amplitude  $E(t)$ , we define the pulse area  $\theta$  as the time integral over the Rabi frequency  $\theta = \int \Omega(t) dt = \frac{\mu}{\hbar} \int E(t) dt$ . This gives a dimensionless quantity  $\theta$  related to the optical input power in the case of a positive-valued pulse shape such as a Gaussian pulse. Without losses a pulse with  $\theta = 2\pi$  leads to a complete *Rabi cycle* of  $p(t)$ . Figure 3(a) shows  $p(t)$  as resulting from an optical input pulse  $E(t)$  (solid red curve) with  $\theta = 2\pi$  for different dephasing times  $T_2$ . While the polarization amplitude for a short dephasing time  $T_2 = 10$  fs (dashed blue line in figure 3(a)) is rapidly damped due to scattering induced dephasing, it shows almost a full *Rabi cycle* for  $T_2 = 150$  fs (dotted black line). The polarization amplitude  $p(t)$  is also rapidly destroyed for a dephasing time of  $T_2 = 25$ , chosen for most of the simulations in this paper, and a pulse area of  $\theta = \pi$  as shown with the dashed blue line in figure 3(b). However, drastically increasing the input pulse area to  $\theta = 4\pi$  leads to a damped *Rabi cycle* as depicted with the dotted black line in figure 3(b).

Figures 4(a) and (b) show the time series of the QD occupation probabilities  $f_e$  and  $f_h$  resulting from the optical input pulse shown in figure 3 (solid red line). At  $t \approx 2$  ps, the light field arrives and both  $f_e$  and  $f_h$  first decrease rapidly due to carrier depletion by stimulated radiative recombination, and finally they asymptotically recover their initial values when the light pulse has passed. The recovery process of electrons is much slower than that of holes as visible by comparing

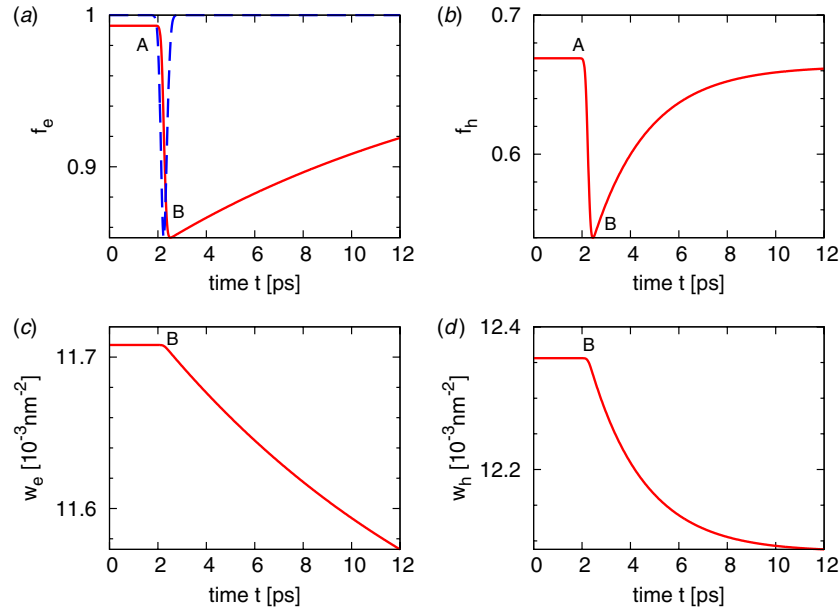


**Figure 4.** Time series of the dynamic variables as resulting from the optical input pulse shown in figure 3. (a), (b) Occupation probabilities  $f_e$  and  $f_h$  in the QD, (c), (d) QW electron and hole density  $w_e$  and  $w_h$ , respectively. The transient behavior of  $p(t)$  is depicted by the dashed blue curve in (a). Parameters:  $\theta = \pi$ ,  $T_2 = 25$  fs,  $j = 20 j_0$ .

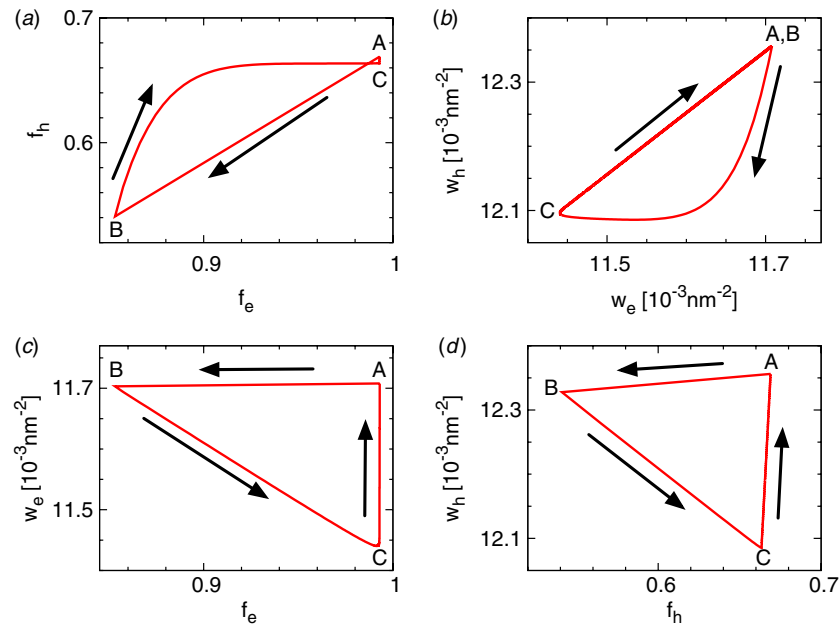


**Figure 5.** Phase space projections of the trajectories resulting from the optical input pulse shown in figure 3. (a)  $(f_e, f_h)$ -plane, (b)  $(w_e, w_h)$ -plane, (c)  $(f_e, w_e)$ -plane and (d)  $(f_h, w_h)$ -plane. The points marked A, B, C correspond to the arrival of the pulse (A), beginning of the QD carrier recovery (B), and complete recovery of QD electrons (C). Time traces between 0 and 10 ns have been used. Parameters:  $\theta = \pi$ ,  $T_2 = 25$  fs,  $j = 20 j_0$ .

figures 4(a) and (b). Figures 4(c) and (d) show time traces of  $w_e$  and  $w_h$  both exhibiting a continuous decrease as soon as the QD carriers start to recombine radiatively. The QW carrier densities are not directly affected by the optical input pulse but change due to their scattering-induced coupling to the QD levels. Therefore, the QW carrier densities decrease further until the pump term in equations (4) and (5) exceeds the depopulation due to refilling of the QD levels. To shed further light on the carrier dynamics, we analyze the trajectories of figure 4 in different phase space projections. Figure 5(a) shows

a plot of  $f_e$  versus  $f_h$  clearly indicating that the dynamics of electrons and holes in the QDs is desynchronized. The points marked A, B, C correspond to the arrival of the pulse (A), beginning of the QD carrier recovery (B), and complete recovery of QD electrons (C), respectively. The times A, B, C are also marked in the transients shown in figure 4. In the case of synchronized dynamics of electrons and holes, the plot would show a single line, instead a bow-like structure is seen in figure 5(a). While the initial depopulation ( $A \rightarrow B$ ) caused by stimulated absorption is of course synchronous, the

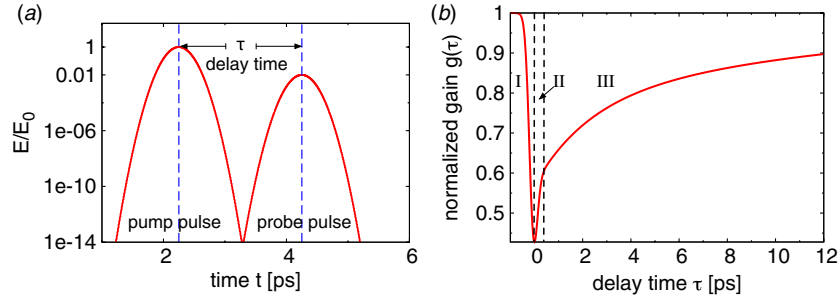


**Figure 6.** (a) Electric field amplitude  $E(t)$  of pump and probe pulse: pump–probe delay time  $\tau$  is the time lag between the peak of the pump pulse  $E_0^{\text{pump}}$  and the peak of the probe pulse  $E_0^{\text{probe}}$ . (b) Normalized gain  $g(\tau)$  calculated from equation (11) as a function of  $\tau$ : different phases of the gain dynamics are (I) gain depletion, (II) ultrafast gain recovery and (III) slow gain recovery. Parameters:  $\theta = \pi$ ,  $T_2 = 25$  fs,  $j = 20j_0$ .

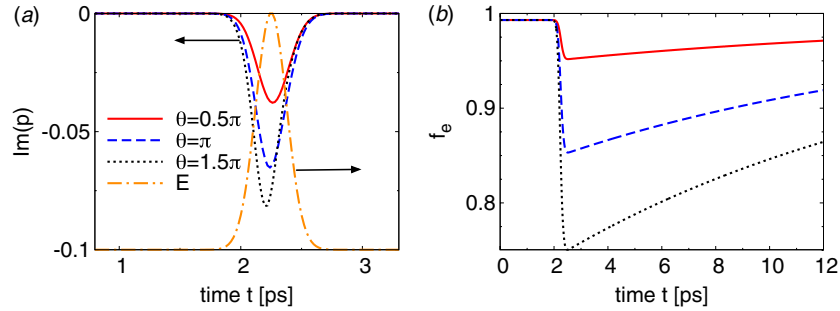


**Figure 7.** Pulse area dependence. Solid red, dashed blue and dotted black curves correspond to transients resulting from optical input pulses (dash-dotted orange curve) of  $\theta = 0.5\pi$ ,  $\theta = \pi$  and  $\theta = 1.5\pi$ , respectively. (a) Microscopic polarization  $p(t)$  and (b) occupation probability of QD electrons  $f_e(t)$ . Parameters:  $j = 20j_0$ ,  $T_2 = 25$  fs.

recovery ( $B \rightarrow C \rightarrow A$ ) is desynchronized. At first the holes recover faster than the electrons, then the relaxation of holes is slowed down ( $B \rightarrow C$ ). At point C, the electron population has reached its initial value and only the hole population still increases to its starting value ( $C \rightarrow A$ ). This part of the relaxation dynamics is very slow ( $>1$  ns). The recovery dynamics for times  $t \gg T_2$ , when the polarization has decayed sufficiently, is governed by the microscopic scattering rates. The desynchronized behavior of electrons and holes in figure 5 is therefore directly linked to the scattering processes. While the in-scattering rates for electrons and holes are approximately of the same order for the given QW densities, the out-scattering rates for holes are orders of magnitude larger than those of electrons (see figure 2(a)) resulting in different relaxation time scales.

Figure 5(b) shows phase portraits projected onto the  $(w_e, w_h)$ -plane. As in figure 5(a), electrons and holes in the QW partly show desynchronized dynamics which is again related to the different time scales induced by the scattering rates. Acting as a reservoir for the localized QD levels, a drain of QW carriers is induced during the transition from B to C in figure 5(b) corresponding to a refill of the QD populations (see figure 5(a)). When the QD levels are refilled sufficiently, the QW dynamics is dominated purely by the injection current which is equal for both electrons and holes ( $C \rightarrow B$  in figure 5(b)). To illustrate the QD QW coupling, figures 5(c) and (d) show phase space projections onto the  $(f_e, w_e)$ - and  $(f_h, w_h)$ -plane, respectively. Both plots have a triangular shape. When the pulse arrives, the QD occupation probabilities decrease ( $A \rightarrow B$ ). Starting from point B, the QD

populations increase while the QW carrier densities decrease. At point C, the occupation probability of electrons has fully recovered. Going from C back to A, only slight changes in the QD hole populations are visible and mainly the QW carriers recover.

To analyze the gain recovery of the amplifier, we have to model the dynamics for a pump and a probe pulse entering the device. Figure 6(a) shows the electric field amplitude  $E(t)$  for a fixed delay time of  $\tau = 2$  ps between the peak of the pump pulse ( $E_0^{\text{pump}}$ ) and the peak of the probe pulse ( $E_0^{\text{probe}}$ ) as a function of time. The ratio between optical pump and probe pulse amplitudes is set to  $E_0^{\text{probe}}/E_0^{\text{pump}} = 0.01$ . The resulting gain calculated from equation (11) is plotted against the pump–probe delay time  $\tau$  in figure 6(b). Here, the gain is normalized to the value at times long before the pump pulse arrives. Figure 6(b) shows three phases of gain dynamics. First, the gain is depleted by the entering pump pulse (I) followed by a phase of ultrafast gain recovery (II) which is related to the coupled dynamics of the QD populations and the microscopic polarization. At last a slow recovery (III) takes place corresponding to the dynamics of the QD and QW charge carriers which is determined by the nonlinear carrier–carrier scattering rates.

### 3.1. Influence of the pulse area

Figure 7(a) shows the imaginary part of the microscopic polarization  $p(t)$  after the interaction of the gain medium with a single optical pulse with different pulse areas  $\theta$ . With increasing  $\theta$ , corresponding to a larger electric field amplitude,

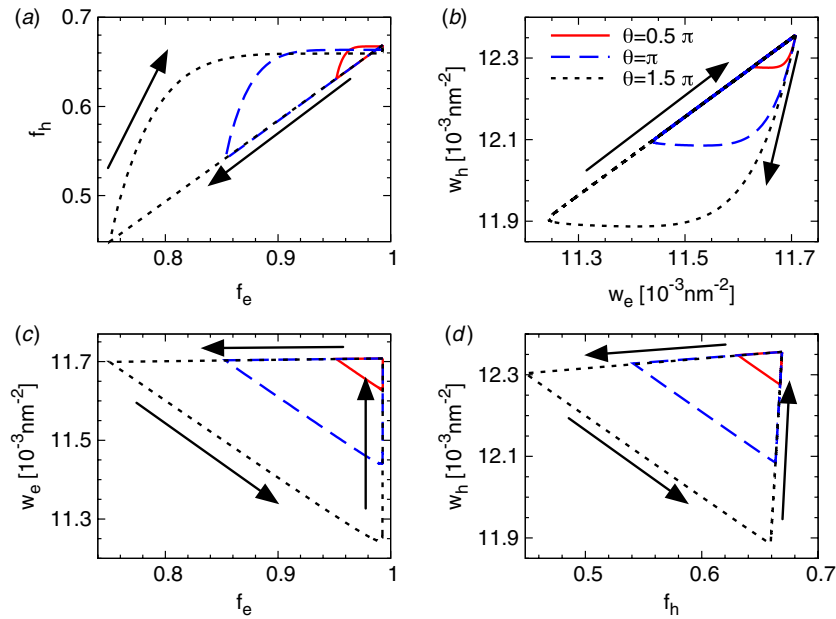


**Figure 8.** Phase space projections. Solid red, dashed blue and black dotted lines depict trajectories resulting from optical input pulses with  $\theta = 0.5\pi, \theta = \pi$  and  $\theta = 1.5\pi$ , respectively. (a)  $(f_e, f_h)$ -plane, (b)  $(w_e, w_h)$ -plane, (c)  $(f_e, w_e)$ -plane and (d)  $(f_h, w_h)$ -plane. Parameters:  $j = 20 j_0, T_2 = 25 fs$ . Time traces between 0 and 10 ns have been used.

$p(t)$  increases and the maximum shifts to smaller times. This effect can be understood by looking at figure 7(b) which shows a plot of the QD electron population for different pulse areas. With increasing  $\theta$ , the carrier populations are depleted more strongly as the pulse interacts with the QD gain medium. Therefore, starting with the arrival of the pulse the associated gradual reduction of the inversion during the passing time of the pulse also becomes stronger for larger input pulses. Since the strength of the light–matter interaction and the induced polarization of the gain medium depend on the population inversion, this effect shifts the peak polarization amplitude toward the leading edge of the optical input pulse where it experiences a larger inversion as shown in figure 7(a).

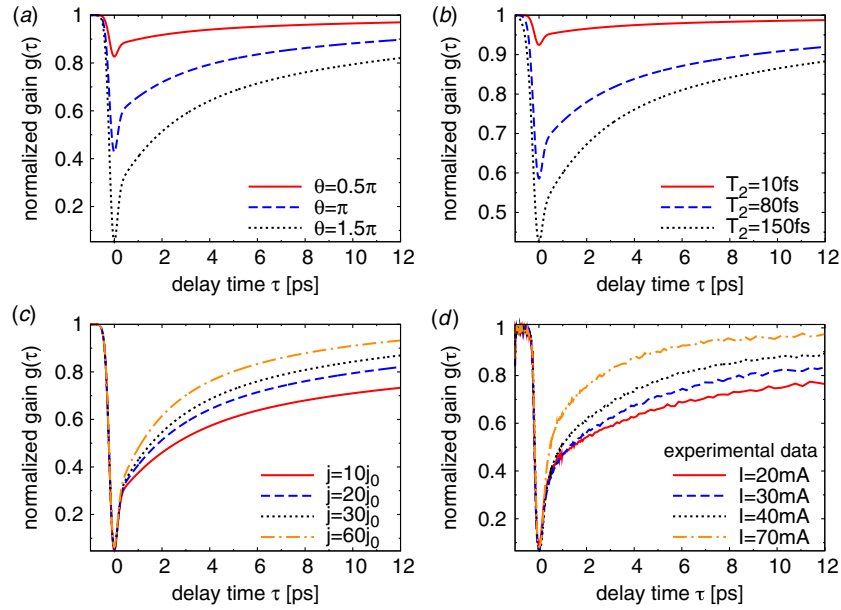
Figure 8 depicts phase portraits of different sections of the phase space showing the trajectory of the dynamic variables after being exposed to a single optical input pulse. To clarify the impact of the pulse area, each plot contains three curves referring to  $\theta = 0.5\pi, \theta = \pi$  and  $\theta = 1.5\pi$  plotted as solid red, dashed blue and dotted black lines, respectively. The qualitative dynamical behavior shown in the phase plots is similar to that discussed in figure 5. We observe that the pulse area scales the phase space trajectories in such a way that for increasing pulse areas the amplitude in phase space is increased.

Figure 9(a) shows the influence of the pulse area on the simulated gain  $g(\tau)$  obtained with equation (11). It can be seen that the magnitude of the gain depletion (indicated by phase I in figure 6(b)) increases with increasing pulse area  $\theta$ . As stated earlier, the pulse area directly corresponds to the optical input power thus allowing a direct comparison with experiments obtained with different optical pump pulses as published by Gomis-Bresco *et al* [7]. In agreement with our results, they found a similar trend for the dependence

of the gain recovery dynamics on the optical pump power. Throughout the literature, the recovery dynamics is often described by recovery time scales that are obtained by linearly fitting a multi-exponential decay. However, we prefer not to extract those times because the highly nonlinear Bloch equation approach combined with the microscopic scattering rates does not yield constant recovery times. Instead they vary with operating conditions (i.e., pump current, pulse area) and constant values would be misleading.

### 3.2. Effect of dephasing time

This section is dedicated to the effects of the dephasing time  $T_2$  on the gain recovery dynamics of QD SOAs. Similarly to the last section, we are going to investigate single pulses and pump–probe configurations with time traces and phase space projections. Figure 10(a) shows the influence of the dephasing time on the imaginary part of the microscopic polarization. For increasing dephasing times, the microscopic polarization amplitude also increases. Increasing dephasing time directly corresponds to lower damping caused by the  $-\frac{1}{T_2}p$  term in the dynamical equation for the polarization (equation (1)), therefore building up a stronger polarization for constant input pulse power. Here, the combination of the input pulse area and  $T_2$  causes a shift of the peak polarization toward the trailing edge of the input pulse, because the polarization is sustained longer and a small input pulse area affects the inversion relatively little within the duration of the pulse. Figure 10(b) depicts the dephasing time dependence of the occupation probability of electrons. The reduction of the QD electron population is enhanced for increasing  $T_2$  due to a stronger light–matter interaction. Figure 11 shows phase space portraits of the dynamic variables while exposed to an



**Figure 9.** (a) Calculated normalized gain  $g(\tau)$  as function of the pump–probe delay time  $\tau$  calculated for different pump pulse areas  $\theta$  depicted as solid red, dashed blue and dotted black curves referring to  $\theta = 0.5\pi$ ,  $\theta = \pi$  and  $\theta = 1.5\pi$ . Parameters:  $j = 20j_0$ ,  $T_2 = 25$  fs. (b) Calculated normalized gain  $g(\tau)$  for varying dephasing times depicted by solid red, dashed blue and dotted black lines referring to  $T_2 = 10$  fs,  $T_2 = 80$  fs and  $T_2 = 150$  fs, respectively. Parameters:  $j = 20j_0$ ,  $\theta = 0.5\pi$ . (c) Calculated normalized gain  $g(\tau)$  for different injection current densities, solid red, dashed blue, dotted black and dash-dotted orange curves referring to  $j = 10j_0$ ,  $j = 20j_0$ ,  $j = 30j_0$  and  $j = 60j_0$ , respectively. Parameters:  $\theta = 1.5\pi$ ,  $T_2 = 25$  fs. (d) Measured gain dynamics for increasing injection currents (transparency current  $I_0 = 5.6$  mA) and an input pulse energy of 0.1 pJ.

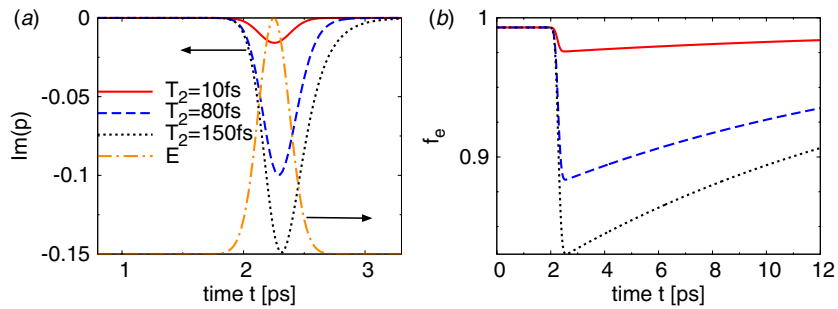


**Figure 10.** Transient behavior of (a) microscopic polarization  $p(t)$  and (b) electron occupation probability in the QD  $f_e(t)$  after being exposed to an optical input pulse with  $\theta = 0.5\pi$  (dash-dotted orange curve). Solid red, dashed blue and black dotted curves correspond to  $T_2 = 10$  fs,  $T_2 = 80$  fs and  $T_2 = 150$  fs, respectively. Parameters:  $j = 20j_0$ .

optical pump pulse. Different sections of the phase space (the same as in figure 5) are displayed for varying dephasing times of  $T_2 = 10$  fs,  $T_2 = 80$  fs and  $T_2 = 150$  fs as solid red, dashed blue and black dotted curves, respectively. The dynamical behavior visible in the phase space projections of figure 11 strongly resembles the dynamics shown in figure 5. Comparing the influence of the dephasing time and the pulse area on the carrier dynamics, we see that variation of both quantities shows the same qualitative effect, namely an enlarged phase space excursion for an increasing value in both cases. The resulting gain recovery dynamics for varying  $T_2$  is shown in figure 9(b). For an increased dephasing time, the gain depletion increases just as in the case of increasing  $\theta$ .

### 3.3. Influence of injection current density

The injection current density used for an electrically pumped QD SOA device also influences the amplifier performance and will be discussed now. Figure 12(a) shows the time series of the microscopic polarization  $p(t)$  if the gain medium is inverted with different injection current densities  $j$  ( $j = 10j_0$ ,  $j = 15j_0$  and  $j = 20j_0$ ), before being exposed to the optical input pulse. It can be seen that the absolute value of the minimum of  $p(t)$  increases with growing injection current density. The reason is that the microscopic polarization depends on the inversion ( $f_e + f_h - 1$ ) (see equation (1)) which is also affected by changes in  $j$ . Figure 12(b) shows time traces of the QD electron occupation probability  $f_e$  for varying injection current density  $j$ . Apparently, with increasing

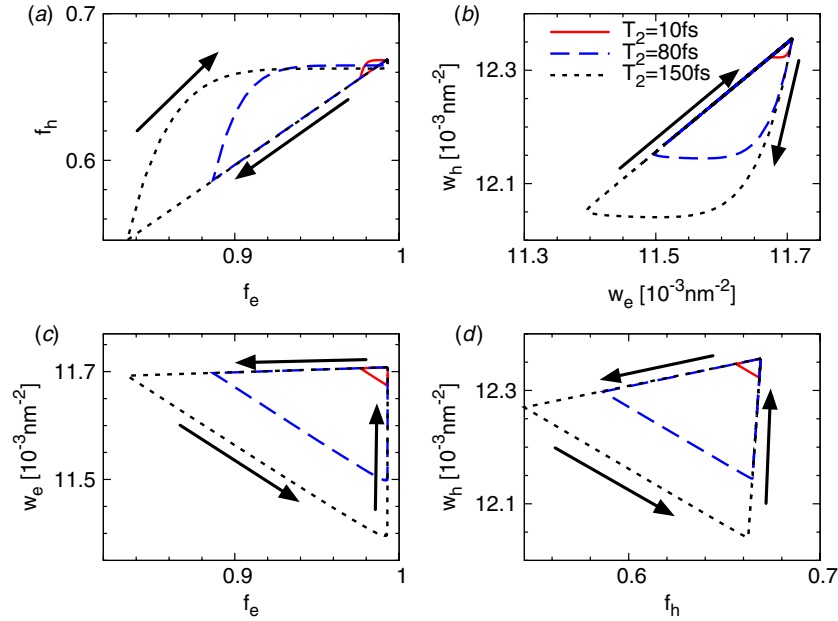


**Figure 11.** Phase space projections in analogy to figure 5 for three different dephasing times  $T_2 = 10$  fs,  $T_2 = 80$  fs and  $T_2 = 150$  fs shown as solid red, dashed blue and dotted black lines, respectively. Parameters:  $j = 20 j_0$ ,  $\theta = 0.5 \pi$ . Time traces between 0 and 10 ns have been used.

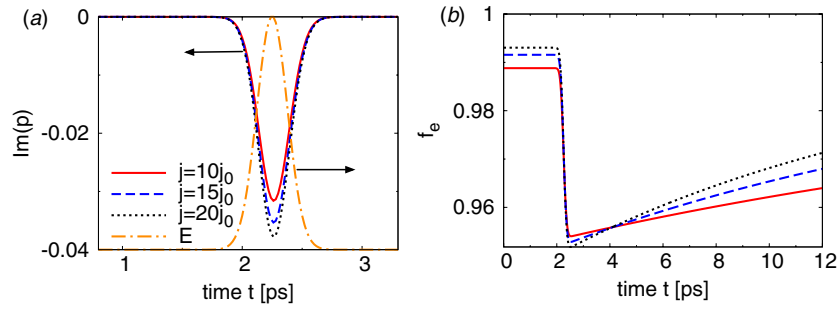


**Figure 12.** Injection current density dependence: (a) imaginary part of the microscopic polarization  $p(t)$ . (b) Occupation probability of electrons in the QD  $f_e(t)$  during arrival of optical input pulse with amplitude  $E(t)$  (dash-dotted orange line in (a)) for three different injection current densities. Solid red, dashed blue, dotted black curves refer to  $j = 10 j_0$ ,  $j = 15 j_0$  and  $j = 20 j_0$ , respectively. Parameters:  $\theta = 0.5 \pi$ ,  $T_2 = 25$  fs.

injection current the QD electron and hole levels are initially more strongly populated due to increased in-scattering into the QDs (see phase plots in figure 13). This in turn leads to a larger population inversion that results in a stronger light–matter interaction depleting more carriers from the QD electron and hole levels. Also, the higher initial carrier depletion reduces the effect of Pauli blocking and therefore increases the recovery rate of the QD carrier population with growing injection current. Note that under variation of the pulse area  $\theta$  or the dephasing time  $T_2$  the initial carrier populations are not affected as shown in figures 7 and 10 in previous sections. In figure 13, we analyze phase portraits of the dynamic variables for different phase space projections after injecting an optical pump pulse as in figures 5 and 11. Each plot contains three curves referring to  $j = 10 j_0$ ,  $j = 15 j_0$  and  $j = 20 j_0$  depicted as solid red, dashed blue and dotted black lines, respectively. Contrary to figures 8 and 11, variation of the injection current density notably affects the initial QD carrier populations and QW carrier densities. Figure 13(a) displays phase space plots in the  $(f_e, f_h)$ -plane for the three

different injection current densities. It can be seen that the initial occupation probabilities are shifted to higher values for increasing injection current densities and also the phase space excursions become slightly larger for an increased injection current. The shift of the initial QD occupation probabilities is stronger for holes since the electrons are already highly filled for small injection current densities.

Figure 13(b) shows the dynamics in the  $(w_e, w_h)$  phase space projection. As mentioned before, a notable increase of both  $w_e$  and  $w_h$  with increasing injection current density can be observed, while only little changes within each phase plot corresponding to different injection currents  $j$  are visible. In figures 13(c) and (d), the trajectories are shown in the  $(f_e, w_e)$  and  $(f_h, w_h)$  phase space projection. Again, we see a drastic change in the QW carrier densities corresponding to different injection currents  $j$  both for electrons and holes, while within each phase plot for fixed  $j$  the QW carrier densities do not vary much. As already shown in figure 12(b) for electrons, we observe significant changes of both  $f_e$  and  $f_h$  for all chosen injection current densities.

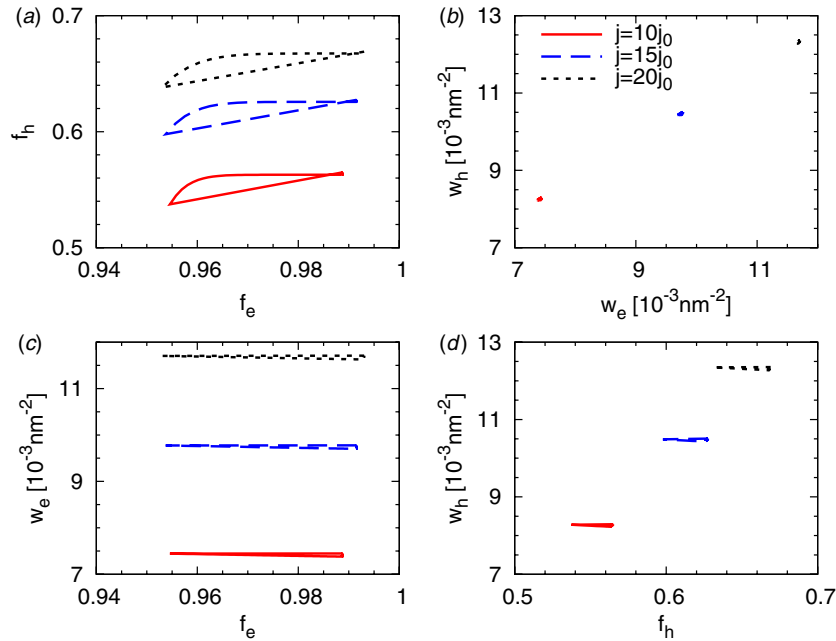


**Figure 13.** Phase space plots of trajectories as shown in figure 5 but for devices inverted with different pump currents. Solid red, dotted blue and dashed black lines correspond to  $j = 10 j_0$ ,  $j = 15 j_0$  and  $j = 20 j_0$ , respectively. Parameters:  $\theta = 0.5 \pi$ ,  $T_2 = 25$  fs. Time traces between 0 and 10 ns have been used.

The resulting gain recovery dynamics under variation of  $j$  is shown in figure 9(c). Apparently the initial gain depletion and the ultrafast gain recovery (indicated by I and II in figure 6(b)) remain almost unchanged under variation of  $j$ . Instead mainly the slow phase of the gain recovery (indicated by III in figure 6(b)) is influenced by  $j$ , showing enhanced recovery for higher injection currents. As discussed before by means of the carrier dynamics, this effect is caused by the nonlinear in-scattering rates plotted in figure 2(a) as they increase with the carrier density in the reservoir. Comparing figure 9(c) with figures 9(a) and (b), where changes in the gain recovery dynamics with  $\theta$  and  $T_2$ , respectively, are plotted, it becomes apparent that the behavior is qualitatively different for varying  $j$ . Figure 9(d) depicts experimental time traces of the normalized single-pass intensity gain of the QD SOA, e.g. the ratio of input and output intensity of the signal, for varying injection currents and an input pulse energy of 0.1 pJ. The theoretically predicted behavior in figure 9(c) nicely resembles the experimental results showing that the gain depletion and the ultrafast gain recovery are unaffected whereas the slow dynamics (non-coherent processes) of the gain recovery accelerates with increasing injection current.

Note that the measured transparency current of the device is  $I_0 = 5.6$  mA, yielding a quantitative discrepancy between simulated and experimental pump currents in figure 9(c) and (d). However, since we do not perform transport simulations and thus neglect effects like leakage currents or space-dependent transport our focus lies on the qualitative comparison. It is also difficult to quantitatively compare the pulse area to the experimental pulse energy. The pulse area is related to the amplitude of the electric field envelope of the optical input pulse. Integrating the resulting energy density

(proportional to the square of the electric field) over the lateral dimension of the waveguide results in an input pulse energy in the order of femto-Joule that enters the active region in our simulations. In the experiments, the focus of the incoming beam is round and bigger than the rectangular active region which makes it hard to estimate the energy that really enters the device.

#### 4. Simulation of pulse trains

For applications in ultrafast optical networks, QD SOAs must be able to amplify femtosecond pulse trains with high repetition rates. To study the potential of QD SOAs for THz pulse train amplification, the gain reduction  $\Delta$  plays a crucial role. The definition of  $\Delta$  is illustrated in the inset of figure 14(b) that displays the measured normalized gain after two optical pulses separated by 1 ps entered the device. Figure 14(a) shows the simulated gain reduction  $\Delta$  as function of the pulse repetition rate for two different pulse areas  $\theta = 0.5 \pi$  (squares) and  $\theta = \pi$  (circles) and two pump currents of  $j = 20 j_0$  (dotted lines) and  $j = 60 j_0$  (solid lines), respectively.  $\Delta$  increases with rising pulse repetition rate. This effect is stronger for larger  $\theta$  because  $\theta$  scales the magnitude of the gain depletion (see figure 9(a)) which yields increased initial gain depletion and gain recovery time for larger  $\theta$ . Consequently, for fixed delay time  $\tau$ , the gain reduction is larger for larger input pulses. Figure 14(b) depicts the measured gain reduction as a function of the pulse repetition rate. In agreement with our theoretical predictions,  $\Delta$  increases for higher pulse repetition rates. Additionally, the simulated results of the gain reduction plotted in figure 14(a) show a strong dependence on the electric pump current such that larger  $j$  leads to significantly smaller gain reduction.

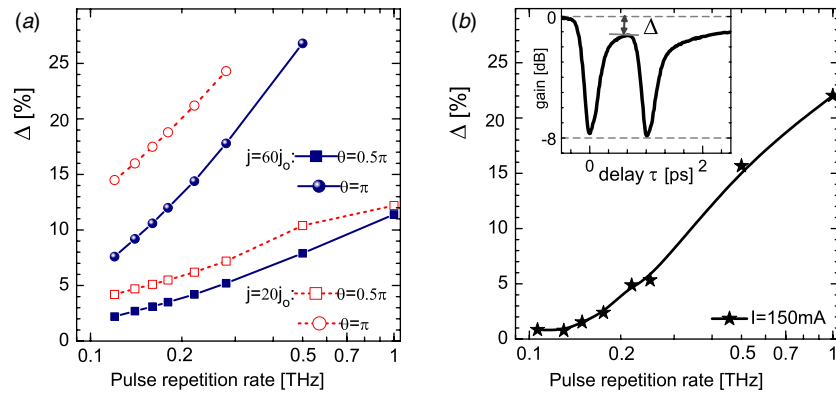


**Figure 14.** (a) Calculated gain reduction  $\Delta$  as a function of the pulse repetition rate for  $\theta = 0.5\pi$  (squares) and  $\theta = \pi$  (circles) for a pump current of  $j = 20j_0$  (dotted lines) and  $j = 60j_0$  (solid lines). Parameters:  $T_2 = 25$  fs (b). Measured gain reduction  $\Delta$  as a function of the pulse repetition rate. Inset: measured normalized gain after the injection of two optical pulses separated by 1 ps illustrating the definition of  $\Delta$  (electric pump current  $I = 150$  mA).

## 5. Conclusion

In conclusion, we have investigated the ultrafast gain recovery dynamics of QD SOAs using an approach based on semiconductor Bloch equations combined with microscopic carrier-carrier scattering between QW and QD states and equations for the QW carrier dynamics. The ultrafast gain depletion was found to be sensitive against changes of the pulse area and the dephasing time of the microscopic polarization, while the injection current density mainly influences the non-coherent (slow) part of the gain recovery dynamics. A detailed analysis of the underlying carrier dynamics using phase space projections revealed desynchronized behavior of electrons and holes in the recovery dynamics of the QD SOA that are directly related to the different microscopic scattering rates. The calculated gain recovery curves show good qualitative agreement with the experimental results found in pump-probe measurements.

## Acknowledgment

This work was supported by DFG in the framework of Sfb787.

## References

- [1] Bimberg D, Grundmann M and Ledentsov N N 1999 *Quantum Dot Heterostructures* (New York: Wiley)
- [2] Akiyama T, Hatori N, Nakata Y, Ebe H and Sugawara M 2003 *Phys. Status Solidi (b)* **238** 301
- [3] Bimberg D and Ledentsov N N 2003 *J. Phys.: Condens. Matter* **15** R1063
- [4] Bimberg D 2005 *J. Phys. D: Appl. Phys.* **38** 2055
- [5] Borri P, Langbein W, Hvam J M, Heinrichsdorff F, Mao M H and Bimberg D 2000 *IEEE Photon. Technol. Lett.* **12** 6
- [6] Chow W W and Koch S W 2004 *Semiconductor-Laser Fundamentals* (Berlin: Springer)
- [7] Gomis-Bresco J, Dommers S, Temnov V V, Woggon U, Lämmlin M, Bimberg D, Malić E, Richter M, Schöll E and Knorr A 2008 *Phys. Rev. Lett.* **101** 256803
- [8] Kim J, Meuer C, Bimberg D and Eisenstein G 2009 *Appl. Phys. Lett.* **94** 041112
- [9] Gomis-Bresco J, Dommers S, Temnov V V, Woggon U, Martinez-Pastor J, Lämmlin M and Bimberg D 2009 *IEEE J. Quantum Electron.* **45** 1121
- [10] Nielsen T R, Gartner P and Jahnke F 2004 *Phys. Rev. B* **69** 235314
- [11] Malić E, Ahn K J, Bormann M J P, Hövel P, Schöll E, Knorr A, Kuntz M and Bimberg D 2006 *Appl. Phys. Lett.* **89** 101107
- [12] Malić E, Bormann M J P, Hövel P, Kuntz M, Bimberg D, Knorr A and Schöll E 2007 *IEEE J. Sel. Top. Quantum Electron.* **13** 1242
- [13] Lüdge K and Schöll E 2009 *IEEE J. Quantum Electron.* **45** 1396
- [14] Lüdge K and Schöll E 2010 *Eur. Phys. J. D* **58** 167
- [15] Otto C, Lüdge K and Schöll E 2010 *Phys. Status Solidi (b)* **247** 829
- [16] van der Poel M, Gehrig E, Hess O, Birkedal D and Hvam J M 2005 *IEEE J. Quantum Electron.* **41** 1115
- [17] Dachner M R et al 2010 *Phys. Status Solidi (b)* **247** 809
- [18] Pikal J M, Menoni C S, Thiagarajan P, Robinson G Y and Temkin H 2000 *Appl. Phys. Lett.* **76** 2659
- [19] Schöll E, Bimberg D, Schumacher H and Landsberg P T 1984 *IEEE J. Quantum Electron.* **20** 394
- [20] Schöll E 1988 *IEEE J. Quantum Electron.* **24** 435